Sustainable Energy Technologies and Assessments 93 (2026) 105312

Contents lists available at ScienceDirect

Sustainable Energy Technologies and Assessments

journal homepage: www.elsevier.com/locate/seta

Original article

Network-aware menu pricing for electric vehicle charging and vehicle-to-grid dispatch under distribution constraints

Lilia Tightiz [a], L. Minh Dang [b,c], Hyosik Yang [a,*]

[a] Department of Computer Engineering, Sejong University, 209, Neungdong-ro, Gwangjin-gu, Seoul, 05006, Republic of Korea
[b] The Institute of Research and Development, Duy Tan University, Da Nang, 550000, Viet Nam
[c] Faculty of Information Technology, Duy Tan University, Da Nang, 550000, Viet Nam

ARTICLE INFO

Keywords:
Electric vehicle charging
Menu-based pricing
Demand response
Vehicle-to-grid integration
Discrete choice modeling

ABSTRACT

An elasticity-aware menu pricing method is proposed for electric vehicle (EV) charge demand and vehicle-to-grid (V2G) dispatch under stochastic demand and feeder constraints. User response, state of charge (SoC)-constrained V2G dispatch, and feeder limits are represented in one optimization model. Price elasticity parameters are estimated from observed EV charge data through a discrete choice model and are used in the joint tariff and dispatch formulation. The large-scale quadratic unconstrained binary optimization (QUBO) model is solved by classical decomposition and mixed-integer quadratic programming (MIQP) refinement. Jeju Island EV station profiles are assigned to the Korea Electric Power Corporation (KEPCO) Active Distribution Test System (KADTS) benchmark feeder through a proportional station-to-node rule. This rule is used as a surrogate because actual feeder geographic information system (GIS) data, telemetry, and station connectivity are unavailable. The actual Jeju feeder and a complete urban transport network (UTN) model are not represented. Feeder values are obtained from LinDistFlow and are interpreted as benchmark-based estimates. Under these assumptions, maximum line loading is limited to 94.3%, SoC-feasible V2G dispatch is retained, and social welfare is increased by 12.8% with stable operator revenue. Mean runtime is reduced by more than 50% relative to the classical MIQP baseline. The maximum objective error due to the five-bit discretization is 0.42% across the 30 daily instances. The value of joint behavioral and feeder-aware tariff design is demonstrated under the adopted benchmark conditions.

Introduction

The rapid electrification of transportation is reshaping both urban mobility and power distribution system operation. As electric vehicle (EV) adoption grows, charging demand becomes increasingly concentrated in time and space, creating operational challenges such as feeder overloading, voltage deviations, and transformer stress during peak periods. At the same time, vehicle-to-grid (V2G) capability allows EV batteries to provide flexible support during high-demand conditions [1]. Charging demand is affected by mobility-related station use and feeder conditions. Cross-domain effects are therefore considered to reduce demand concentration at mobility hotspots and inefficient tariff signals [2]. However, traffic flow, route choice, and UTN constraints are not represented in this study.

Dynamic pricing is widely used to coordinate EV demand with grid conditions [3,4]. A choice among charge and discharge contracts with different prices, deadlines, and flexibility levels is provided by menu-based pricing [5,6]. A large combinatorial problem is produced by the joint representation of mobility-informed station demand, user elasticity, V2G participation, and feeder constraints [7,8]. Such problems can be represented as QUBO models and can be solved by classical or quantum-compatible methods [9,10]. In this study, the QUBO formulation is treated as a hardware-compatible mathematical representation. Large-scale quantum computation is not claimed.

The Jeju Island EV DR dataset [11] is used for the empirical demand profiles. These station profiles are allocated to the KADTS benchmark feeder [12] through a proportional station-to-node rule based on peak demand. This allocation is used as a surrogate because actual feeder GIS, telemetry, and station connectivity data are unavailable. Traffic assignment, road topology, route choice, and travel-time constraints are not included. Therefore, a comprehensive UTN–power distribution network (PDN) model is not claimed.

Q-MENU-PDN is proposed as a joint EV menu pricing model. Elasticity-aware demand, SoC-feasible V2G dispatch, and LinDistFlow constraints are represented at the same decision level. The method

* Corresponding author.
E-mail address: hsyang@sejong.edu (H. Yang).

https://doi.org/10.1016/j.seta.2026.105312
Received 10 May 2026; Received in revised form 30 July 2026; Accepted 8 August 2026
Available online 24 August 2026

is assessed under empirical station demand and a benchmark radial feeder. Actual feeder GIS, telemetry, and station connectivity data are required for direct use by operators such as KEPCO.

The main contributions of this work are as follows:

- **PDN-aware menu pricing:** Menu prices are optimized subject to LinDistFlow voltage, line-capacity, and transformer constraints. Feasibility is defined with respect to the adopted linear feeder model.
- **Elasticity-aware demand model:** Heterogeneous price, deadline, and incentive responses are represented through an MNL model.
- **SoC-feasible V2G integration:** V2G participation is constrained by battery SoC and station discharge limits.
- **QUBO-based hybrid optimization:** Menu prices and V2G credits are encoded in QUBO form. Full-scale cases are solved by classical decomposition and MIQP refinement. Reduced cases are used for hardware compatibility tests.
- **Mobility-informed station-to-feeder assignment:** Empirical station-level charge profiles are assigned to benchmark feeder nodes. This assignment permits an assessment of tariff and feeder interactions under spatially concentrated demand. It is treated as a surrogate and not as a complete UTN–PDN model.

Related work

Research on EV charging pricing and demand management has expanded rapidly with the growth of electric mobility and the need to coordinate charging demand with grid operation. Existing studies have explored several approaches, including menu-based tariffs, dynamic pricing, and game-theoretic mechanisms that integrate charging infrastructure with renewable energy and storage systems. A key challenge in this literature is simultaneously addressing heterogeneous user behavior, network operational limits, and economically efficient pricing mechanisms.

Menu-based pricing has been widely studied as a mechanism to capture differences in user flexibility and willingness to pay. Lu et al. [5] introduced deadline-differentiated charging menus that allow users to reveal their charging flexibility, improving welfare relative to flat or time-of-use (ToU) tariffs. Subsequent work has explored adaptive menu designs and multi-service charging stations that incorporate different charging modes and queueing dynamics [13,14]. While these studies demonstrate the effectiveness of menu-based tariffs for demand management, they typically do not incorporate explicit distribution network feasibility constraints.

Accurate estimation of demand elasticity is also essential for realistic tariff design. Data-driven studies have estimated elasticity parameters from historical charging data to improve demand response (DR) and pricing strategies [15,16]. Empirical evidence from Korea further indicates that fixed charging tariffs often lead to economically inefficient operation of public charging infrastructure [17]. In parallel, stochastic and dynamic pricing frameworks have been proposed to account for uncertainty in charging demand and renewable generation [18–20]. However, many of these approaches treat grid constraints, V2G participation, and behavioral demand modeling as separate components rather than integrating them within a unified optimization framework.

Network-aware charging strategies have also been investigated using power system optimization and learning-based methods. For example, Cui et al. [21] proposed a bi-level pricing framework based on distribution locational marginal prices (DLMPs) to coordinate charging networks and distribution systems. Reinforcement learning approaches have further been applied to dynamic EV pricing, modeling tariff design as a Markov decision process and leveraging deep learning techniques to improve operator revenue [22,23]. Although these methods capture complex user behavior, they typically rely on centralized optimal power flow or end-to-end learning policies without explicitly constructing user-facing menu options under feeder-level feasibility constraints.

A broad basis for QUBO and quantum annealing (QA) in energy optimization is provided by Ajagekar et al. [24]. Facility location, unit commitment (UC), and heat exchanger network synthesis (HENS) problems are solved on quantum and classical hardware. QUBO reformulation, discretization, and QA execution are examined. Limits due to qubit connectivity, minor embedding, coefficient precision, and problem scale are also identified. A wider review of quantum computing (QC) and quantum AI for renewable and sustainable energy is provided in [25]. Applications in optimization, machine learning (ML), and sustainable energy materials are assessed. Realistic limits of current quantum devices are also emphasized.

Hybrid QC methods for large discrete-continuous problems are proposed by Ajagekar et al. [26]. Molecular conformation, job-shop schedules, manufacturing cell formation, and vehicle routing are treated through quantum and classical decomposition. The discrete QUBO subproblems are assigned to QA, while continuous variables and feasibility checks are assigned to classical solvers. However, EV tariff menus, demand elasticity, V2G, and feeder constraints are not addressed in these studies.

Recently, quantum and quantum-inspired optimization techniques have been explored for combinatorial EV charging problems. Dalyac et al. [27] investigated quantum approximate optimization algorithms for charging station scheduling, while Veshchezerova et al. [9] formulated EV fleet scheduling as a QUBO problem solvable via quantum annealing. Sakib et al. [28] further demonstrated city-scale charging infrastructure optimization using D-Wave hardware. Nevertheless, existing studies typically focus on scheduling or infrastructure planning and do not jointly address elasticity-aware menu pricing, SoC-constrained V2G dispatch, and explicit distribution network feasibility within a unified formulation.

Real-time charger allocation is studied by Xu et al. [29] through quantum reinforcement learning (QRL). ToU prices, limited AC-II and direct current fast charging (DCFC) chargers, user urgency, service time, service success, and operator cost are included. Faster convergence and lower parameter demand than classical DRL are reported. However, feeder constraints, bidirectional V2G, elasticity, and tariff-menu selection are not represented.

Residential EV charge and discharge schedules are formulated as QUBO by Deng et al. [30]. ToU prices, household occupancy, battery limits, and D-Wave execution are included. Cases with 225 and 1000 households are evaluated. Peak-load reduction and electricity-cost reduction are reported. However, a fixed ToU tariff is assumed. Elasticity-based menu choice, nodal voltage limits, power-balance equations, and line-capacity limits are not included.

V2G and mobile charge asset placement for disaster relief are reviewed by Christeson et al. [31]. Classical optimization, stochastic methods, reinforcement learning (RL), and metaheuristics are compared. QUBO forms for QA and the quantum approximate optimization algorithm (QAOA) are also presented. Relative to Xu et al. [29], the proposed model is not based on QRL and is not limited to charger allocation. Relative to Deng et al. [30], elasticity-based menu choice and feeder equations are added. Relative to Christeson et al. [31], a tested optimization model is provided rather than a conceptual review. Relative to Refs. [24–26], the QUBO is specialized for EV tariff menus, SoC-feasible V2G, and distribution network operation.

In the reviewed literature, four elements are not jointly represented: elasticity-aware response to discrete tariff menus; endogenous user menu choice; SoC-feasible bidirectional EV operation; and LinDistFlow voltage, nodal balance, and line-capacity limits. In the present work, these elements are encoded in one QUBO model. User economics and feeder feasibility are optimized at the same decision level. The main novelty lies in this joint representation. The model is assessed through a benchmark feeder and a surrogate station-to-node assignment. A complete UTN model is not claimed. A clear distinction from prior charge-schedule, charger-allocation, infrastructure, and broad energy QC studies is therefore provided.

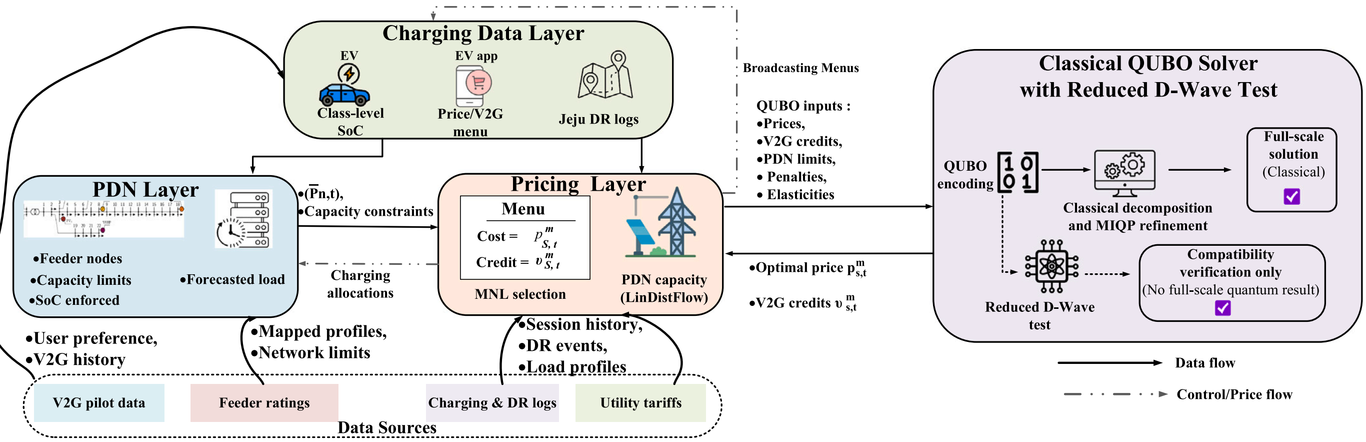

Fig. 1. Q-MENU-PDN architecture with classical full-scale QUBO solution and reduced D-Wave compatibility tests for $q \leq 300$.

PDN-constrained pricing and QUBO formulation

A joint EV menu pricing model is presented under distribution network constraints and battery-constrained V2G participation. LinDistFlow feasibility, aggregated SoC-constrained V2G dispatch, and elasticity-aware menu demand are represented in one optimization formulation. The behavioral parameters are calibrated from the Jeju Island Plus DR EV charge dataset [11].

The station demand profiles are later assigned to the KADTS feeder through a benchmark station-to-node rule. This assignment is used as a surrogate. Traffic flow, route choice, travel time, and UTN constraints are not represented. The stochastic mixed-integer model is reformulated in QUBO form. Full-scale cases are solved mainly by classical decomposition and MIQP refinement. Fig. 1 presents the structure of Q-MENU-PDN.

System description and distribution network model

A set of public EV charge stations is indexed by $s \in \mathcal{S}$. A radial distribution network is denoted by $\mathcal{G} = (\mathcal{N}, \mathcal{L})$, where $\mathcal{N}$ denotes feeder nodes and $\mathcal{L}$ denotes distribution lines.

A modified 42-bus KADTS topology is adopted [12]. The representative load-node set is defined as

$$\mathcal{N}_{\mathrm{L}} = \{3, 4, 16, 22, 34, 43, 53\} \subseteq \mathcal{N}. \tag{1}$$

A representative load node is defined as a benchmark node at which aggregate EV demand is placed. It does not denote an observed connection point for a Jeju station.

Each station s is assigned to one node $n(s) \in \mathcal{N}_{\mathrm{L}}$. The assignment rule is stated in Section "Experimental Setup". The assignment is fixed for all time intervals. It is treated as a surrogate station-to-feeder association. Feeder GIS, station connectivity, geographic distance, road topology, traffic flow, route choice, and travel time are not used. No explicit UTN optimization is performed.

Time is divided into 15-minute intervals $t = 1, \ldots, T$, consistent with the Jeju dataset [11]. At each station and time interval, a menu of K charge contracts is offered:

$$\mathcal{M}_{s,t} = \{(p^m_{s,t}, \tau^m_{s,t}, v^m_{s,t}) \mid m = 1, \ldots, K\},$$

where $p^m_{s,t}$ denotes the charge price, $\tau^m_{s,t}$ denotes the promised completion time, and $v^m_{s,t}$ denotes the V2G discharge credit.

LinDistFlow feasibility is imposed on the benchmark radial feeder. For each line $(i,j) \in \mathcal{L}$ and time interval t, active power flow and voltage drop are represented as

$$P_{ij,t} = \sum_{k \in \mathcal{D}(j)} P_{k,t}, \tag{2}$$

$$V_{j,t} = V_{i,t} - 2(R_{ij} P_{ij,t} + X_{ij} Q_{ij,t}), \tag{3}$$

where $\mathcal{D}(j)$ denotes the set of downstream nodes of node j. Voltage limits are imposed at each node:

$$V_{\min} \leq V_{n,t} \leq V_{\max}, \qquad \forall n \in \mathcal{N},\ t. \tag{4}$$

Line and transformer limits are imposed in apparent-power form:

$$P^2_{ij,t} + Q^2_{ij,t} \leq (S^{\max}_{ij})^2, \qquad \forall (i,j) \in \mathcal{L},\ t, \tag{5}$$

$$P^2_{\mathrm{root},t} + Q^2_{\mathrm{root},t} \leq (S^{\max}_{\mathrm{tr}})^2, \qquad \forall t. \tag{6}$$

A fixed high-power-factor assumption is adopted. Reactive power is represented as proportional to active power. The net active demand at node n is defined as

$$P_{n,t} = P^{\mathrm{base}}_{n,t} + \sum_{s \in \mathcal{S}(n)} \left(\sum_{m=1}^{K} d^m_{s,t} - P^{\mathrm{V2G}}_{s,t} \right), \tag{7}$$

where $P^{\mathrm{base}}_{n,t}$ denotes non-EV baseline demand, $d^m_{s,t}$ denotes the demand assigned to contract m, and $P^{\mathrm{V2G}}_{s,t}$ denotes aggregated station-level discharge power.

The model captures the feeder effects of empirical station demand under the surrogate station-to-node assignment. The actual Jeju feeder topology is not reconstructed. AC phase imbalance, nonlinear AC power flow, traffic flow, route choice, and travel constraints are not represented. These assumptions define the scope of the benchmark assessment.

Elasticity-calibrated demand model with embedded uncertainty

Let $D^{\mathrm{total}}_{s,t}$ denote the observed aggregate charging demand at station s and time interval t from the Jeju Island Plus DR dataset [11]. Let $h(s) \in \mathcal{H}$ denote the behavioral user class assigned to station s. User choice among the K menu contracts is represented through a multinomial logit (MNL) model.

The remaining completion time associated with option m is defined as

$$\Delta\tau^m_{s,t} = \tau^m_{s,t} - t. \tag{8}$$

The systematic utility of menu option m is

$$V^{m,h(s)}_{s,t} = -\alpha_{h(s)} p^m_{s,t} + \beta_{h(s)} v^m_{s,t} - \delta_{h(s)} \Delta\tau^m_{s,t}, \tag{9}$$

where $\alpha_{h(s)}$, $\beta_{h(s)}$, and $\delta_{h(s)}$ denote, respectively, the sensitivities of behavioral class $h(s)$ to the charging price, V2G credit, and remaining completion time. The corresponding random utility is

$$U^{m,h(s)}_{s,t} = V^{m,h(s)}_{s,t} + \varepsilon^m_{s,t}, \tag{10}$$

where $\varepsilon^{m}_{s,t}$ is an independent and identically distributed Type-I extreme-value error term.

The probability that a user belonging to class $h(s)$ selects option m is

$$\pi^{m,h(s)}_{s,t} = \frac{\exp\left(V^{m,h(s)}_{s,t}\right)}{\sum_{m'=1}^{K} \exp\left(V^{m',h(s)}_{s,t}\right)}. \quad (11)$$

For notational simplicity, the behavioral-class index is suppressed below, such that $\pi^{m}_{s,t} \equiv \pi^{m,h(s)}_{s,t}$. The demand allocated to option m is therefore

$$d^{m}_{s,t} = \pi^{m}_{s,t} D^{\text{total}}_{s,t}. \quad (12)$$

Because individual contract choices are not directly observed in the dataset, the elasticity parameters are estimated from reconstructed aggregate market shares. Let $\tilde{s}^{m}_{s,t}$ denote the reconstructed share of option m at station s and time t, obtained by matching the observed tariff and incentive conditions to the closest feasible menu attributes. The reconstructed shares are normalized as

$$\tilde{s}^{m}_{s,t} = \frac{w^{m}_{s,t}}{\sum_{m'=1}^{K} w^{m'}_{s,t}}. \quad (13)$$

The weights $w^{m}_{s,t}$ are constructed from observed station-level charging volumes under historical tariff and DR incentive conditions and are assigned to the closest feasible menu attributes. This reconstruction enables estimation of the MNL parameters when explicit individual contract-choice observations are unavailable.

The class-specific parameters are estimated by maximizing the aggregate fractional log-likelihood:

$$\mathcal{L} = \sum_{s\in S} \sum_{t=1}^{T} \sum_{m=1}^{K} \tilde{s}^{m}_{s,t} \ln\left(\pi^{m}_{s,t}\right). \quad (14)$$

Parameter identification uses records from October 2021 to June 2022. Behavioral user classes are derived from station-level clusters based on charger type, session duration, and DR participation frequency. Historical tariff and DR records are assigned to the closest feasible menu option, and the observed charging volume is used as $w^{m}_{s,t}$. Constrained maximum-likelihood estimation is applied subject to

$$\alpha_h > 0, \qquad \beta_h > 0, \qquad \delta_h > 0, \qquad \forall h \in \mathcal{H}. \quad (15)$$

Standard errors are obtained from the inverse observed Hessian. Model estimation and validation performance are reported in Section "Results".

To represent demand uncertainty, total demand is expressed through a finite scenario set $\omega \in \Omega$:

$$D^{\omega}_{s,t} = \hat{D}_{s,t}\left(1 + \xi^{\omega}_{s,t}\right), \quad (16)$$

where $\hat{D}_{s,t}$ is the point forecast and $\xi^{\omega}_{s,t}$ is sampled from the empirical forecast-residual distribution. The scenario-dependent demand allocated to menu option m is then

$$d^{m,\omega}_{s,t} = \pi^{m}_{s,t} D^{\omega}_{s,t}. \quad (17)$$

Battery-constrained EV class model and aggregated V2G representation

Because vehicle-specific battery and mobility data are absent from the Jeju dataset, aggregate V2G capability is represented by four EV classes. The battery and power parameters are obtained from South Korean market data and official vehicle specifications [32–40]. The class weights are calibrated from South Korean EV registration and model-distribution evidence. Higher weights are assigned to crossover and SUV classes due to their larger market presence. Table 1 reports the adopted parameters and base weights.

The adopted class weights are $\rho_c = \{0.20, 0.35, 0.15, 0.30\}$ for compact BEV, mid-size crossover, sedan BEV, and SUV BEV, respectively [32,41,42]. The weights satisfy

$$\sum_{c\in C} \rho_c = 1. \quad (18)$$

Let $N_{s,t}$ denote the total number of active EVs at station s and interval t. The active number of EVs in class c is defined as

$$N^{c}_{s,t} = \rho_c N_{s,t}. \quad (19)$$

The adopted class weights and vehicle parameters represent the South Korean base case. They are not assumed to represent all EV markets. Application to another market requires local class shares, battery capacities, charge limits, discharge limits, and V2G regulations. No change to the mathematical formulation is required after these parameters are replaced.

For $N^{c}_{s,t} > 0$, the class-average SoC is defined as

$$SoC^{c}_{s,t+1} = SoC^{c}_{s,t} + \eta^{\text{ch}}_{c} \frac{P^{\text{ch},c}_{s,t}\Delta t}{N^{c}_{s,t} E^{\max}_{c}} - \frac{1}{\eta^{\text{dis}}_{c}} \frac{P^{\text{dis},c}_{s,t}\Delta t}{N^{c}_{s,t} E^{\max}_{c}}, \quad (20)$$

When $N^{c}_{s,t} = 0$, both charge and discharge powers are set to zero. The SoC limits are defined as

$$SoC^{\min}_{c} \le SoC^{c}_{s,t} \le SoC^{\max}_{c}. \quad (21)$$

The controllable SoC range is set to $[20\%, 90\%]$ [43].

Aggregate discharge is restricted by effective availability, inverter capacity, and stored energy:

$$0 \le P^{\text{dis},c}_{s,t} \le a^{c}_{s,t} N^{c}_{s,t} P^{\text{dis,max}}_{c}, \quad (22)$$

$$P^{\text{dis},c}_{s,t}\Delta t \le a^{c}_{s,t} N^{c}_{s,t} \left(SoC^{c}_{s,t} - SoC^{\min}_{c}\right) E^{\max}_{c}. \quad (23)$$

Total station-level V2G injection is defined as

$$P^{\text{V2G}}_{s,t} = \sum_{c\in C} P^{\text{dis},c}_{s,t}. \quad (24)$$

The effects of lower availability and alternative class weights are assessed in Section "Robustness and sensitivity analysis". Trip chains are not represented explicitly. Battery degradation cost is included only in the sensitivity analysis in Section "Robustness and sensitivity analysis" and is not included in the main optimization model. The reported V2G energy is therefore interpreted as an aggregate estimate under the adopted class and availability assumptions.

Integrated objective function and grid reliability metrics

The operator selects menu prices and V2G credits to maximize expected economic benefit while feeder reliability and battery feasibility are preserved. The objective includes expected operator margin, consumer surplus, voltage-risk penalty, line-loading penalty, transformer-loading penalty, and revenue-risk penalty:

$$\max\ \mathbb{E}_{\omega}[R^{\omega} - C^{\omega}] + CS - \left(\lambda_{\text{volt}}\Phi_{\text{volt}} + \lambda_{\text{thermal}}\Phi_{\text{thermal}} + \lambda_{\text{tr}}\Phi_{\text{tr}}\right)$$
$$-\ \kappa\, \text{Var}_{\omega}[R^{\omega} - C^{\omega}]. \quad (25)$$

Here, R^{ω} denotes charging revenue, C^{ω} denotes procurement cost, CS denotes aggregate consumer surplus, and Φ_{volt}, Φ_{thermal}, and Φ_{tr} denote voltage, line-loading, and transformer-loading penalties, respectively. Additional objective-function details are provided in Appendix "QUBO reformulation". The penalty coefficients λ_{volt}, λ_{thermal}, λ_{tr}, and κ are calibrated in the experimental setup.

Table 1
Representative EV classes, battery parameters, and base class weights for the South Korean case.

Class	$E_c^{\max}$ (kWh)	$P_c^{\mathrm{ch,max}}$ (kW)	$P_c^{\mathrm{dis,max}}$ (kW)	ρ_c	Representative models
Compact BEV	35–65	7–11	3.5	0.20	Kia Ray EV; Hyundai Kona Electric
Mid-size crossover	72–77	11	3.5–3.6	0.35	Hyundai IONIQ 5; Kia EV6
Sedan BEV	60–75	7–11	0–7	0.15	Hyundai IONIQ 6; Tesla Model 3
SUV BEV	75–82	7–11	0–7	0.30	Tesla Model Y; Kia EV9
Total	–	–	–	**1.00**	–

QUBO reformulation and hardware-compatible binary encoding

The stochastic mixed-integer formulation in Section "Integrated objective function and grid reliability metrics" is reformulated as a QUBO to support scalable combinatorial search and compatibility with quantum optimization hardware. Menu prices and V2G credits are encoded by binary variables, and nonlinear economic, reliability, and risk terms are converted into quadratic penalty terms. The final minimization-compatible QUBO is expressed as

$$Q_{\mathrm{total}} = Q_{\mathrm{econ}} + \lambda_{\mathrm{volt}} Q_{\mathrm{volt}} + \lambda_{\mathrm{thermal}} Q_{\mathrm{thermal}} + \lambda_{\mathrm{tr}} Q_{\mathrm{tr}} + \kappa Q_{\mathrm{risk}}. \tag{26}$$

Additional QUBO encoding details are provided in Appendix "QUBO reformulation". Large-scale instances are solved by classical QUBO decomposition. Validation-scale cases are embedded on quantum annealing hardware only to confirm binary-encoding feasibility. No claim of computational quantum advantage is made.

Classical QUBO solution and reduced D-wave test

The solution process is conducted in five steps. First, stochastic demand scenarios are generated from empirical residual distributions. Second, menu prices and V2G credits are discretized. Third, the objective and constraints are assembled in QUBO form. Fourth, large-scale instances are solved by classical QUBO decomposition and local search. Fifth, the binary solution is refined by MIQP to reduce residual constraint violations and improve the penalized objective. Because the network and SoC violations are penalized rather than guaranteed to be eliminated in every interval, the refinement does not provide an all-interval hard-feasibility guarantee. Final constraint satisfaction is therefore evaluated separately using the original LinDistFlow and SoC limits.

Experimental setup

Dataset and data preparation

The proposed method is evaluated with the Jeju Island Plus DR EV Charging Dataset [11]. The dataset is released by KEPCO and Jeju Energy Corporation. Station metadata, 15-minute charge records, and 77 DR events are included. The observation period extends from October 2021 to December 2022.

A total of 873 registered stations is identified. The retained station set is defined from the DR performance records. Let $R_{s,e}$ denote the recorded DR performance of station s at record e. The number of positive DR records is defined as

$$N_s^{\mathrm{DR}} = \sum_{e\in\mathcal{E}_s} \mathbb{I}\left(R_{s,e} > 0\right), \tag{27}$$

where $\mathbb{I}(\cdot)$ denotes the indicator function. A station is retained when at least six positive DR records are available. The retained set is therefore defined as

$$\mathcal{S} = \left\{s : N_s^{\mathrm{DR}} \geq 6\right\}, \qquad |\mathcal{S}| = 534. \tag{28}$$

All timestamps are converted to KST. All records are aligned to 15-minute intervals. Records with absent energy values, negative durations, or inconsistent timestamps are removed. A total of 1.8% of the records is removed.

Energy is aggregated for each station and interval. Let $E_{s,t}$ denote the energy recorded in kWh during one 15-minute interval. The interval duration is set to $\Delta t = 0.25$ h. The interval-average demand is defined as

$$D_{s,t}^{\mathrm{total}} = \frac{E_{s,t}}{\Delta t} = 4E_{s,t}, \tag{29}$$

where $D_{s,t}^{\mathrm{total}}$ is expressed in kW. The empirical station peak is defined as

$$D_s^{\mathrm{peak}} = \max_{t=1,\ldots,T} D_{s,t}^{\mathrm{total}}. \tag{30}$$

Surrogate station-to-feeder assignment

Because direct KEPCO feeder GIS, telemetry, and station connectivity data are unavailable, the 534 station profiles are assigned to the representative KADTS load-node set $\mathcal{N}_{\mathrm{L}}$.

The 100 MW KADTS case is adopted as the reference case [12]. A reference load of 25 MW is assigned to each of nodes 3 and 4. A reference load of 10 MW is assigned to each of nodes 16, 22, 34, 43, and 53. The reference load is therefore defined as

$$L_n^{\mathrm{ref}} = \begin{cases} 25\ \mathrm{MW}, & n \in \{3,4\}, \\ 10\ \mathrm{MW}, & n \in \{16,22,34,43,53\}. \end{cases} \tag{31}$$

The node weight is defined as

$$w_n = \frac{L_n^{\mathrm{ref}}}{\sum_{j\in\mathcal{N}_{\mathrm{L}}} L_j^{\mathrm{ref}}}. \tag{32}$$

The total reference load is 100 MW. Therefore,

$$w_3 = w_4 = 0.25, \qquad w_{16} = w_{22} = w_{34} = w_{43} = w_{53} = 0.10. \tag{33}$$

The number of stations assigned to each node is obtained through the largest-remainder rule. The initial quota is defined as

$$q_n^0 = \lfloor |\mathcal{S}| w_n \rfloor. \tag{34}$$

The initial quotas provide 531 assignments. The three residual assignments are allocated according to the largest decimal residual. A tie is resolved by the lowest node number. The final quotas are

$$q_3 = q_4 = 134, \qquad q_{16} = 54, \qquad q_{22} = q_{34} = q_{43} = q_{53} = 53. \tag{35}$$

The station list is ordered by decreasing D_s^{peak}. Equal peak values are ordered by ascending customer ID. Let s_k denote the station at position k in this ordered list. Let $\mathcal{S}_n^{k-1}$ denote the station set assigned to node n before station s_k is assigned. The cumulative peak at node n is defined as

$$A_n^{k-1} = \sum_{r\in\mathcal{S}_n^{k-1}} D_r^{\mathrm{peak}}. \tag{36}$$

The eligible node set is defined as

$$\mathcal{N}_k^{\mathrm{E}} = \left\{n \in \mathcal{N}_{\mathrm{L}} : |\mathcal{S}_n^{k-1}| < q_n\right\}. \tag{37}$$

Station s_k is assigned to the eligible node with the lowest weight-adjusted cumulative peak:

$$n(s_k) = \arg\min_{n\in\mathcal{N}_k^{\mathrm{E}}} \left[\frac{A_n^{k-1} + D_{s_k}^{\mathrm{peak}}}{w_n}\right]. \tag{38}$$

A tie in Eq. (38) is resolved by the lowest node number. No separate normalization is applied to D_s^{peak}. The raw peak values are used. The KADTS node base demand is not used as an assignment weight. Only the reference loads in Eq. (31) are used.

Geographic distance, station coordinates, road topology, traffic flow, route choice, and actual feeder connectivity are not used. Charger type is not used for the station-to-node assignment. Charger type is used only as a forecast input.

The station-to-node association is fixed after the assignment. The same association is used for all 15-minute intervals. Aggregate EV demand at node n is defined as

$$P_{n,t}^{\text{EV}} = \sum_{\substack{s\in S\\ n(s)=n}} D_{s,t}^{\text{total}}. \tag{39}$$

This assignment is treated as a surrogate station-to-feeder association. The actual electrical connections of the Jeju stations are not represented. No explicit UTN optimization is performed. The reported feeder values are conditional on the assignment in Eq. (38) and the adopted LinDistFlow assumptions. The KADTS branch parameters are adopted for the feeder assessment. The voltage limits are set to $V_{\min} = 0.95$ p.u. and $V_{\max} = 1.05$ p.u. Line limits are denoted by $S_{ij}^{\max}$. Transformer capacity is denoted by $S_{\text{tr}}^{\max}$.

The node weights, station quotas, and assignment procedure are reported in Appendix "Station-to-feeder assignment details".

Demand forecast and uncertainty

Station-level demand forecasts are produced by GBR and RFR. Hour of day, day of week, demand lags from $t-1$ to $t-8$, DR event indicators, charger type, and weather data are used as inputs.

Chronological order is used for all data splits. Five sequential-origin validation folds are used. Each validation interval is placed after its model-fit interval. Data preparation, feature selection, and parameter selection are restricted to the model-fit period. Test records are excluded from model selection.

Only weather data available at the decision time are used. Future observed weather values are excluded.

GBR and RFR are compared by mean validation RMSE. GBR is selected based on the lowest mean validation RMSE. The selected parameters are reported in Appendix "Forecast model details". The GBR forecast is used as $\hat{D}_{s,t}$ in the optimization model.

Demand uncertainty is represented by $|\Omega| = 20$ scenarios. The scenarios are formed from sampled forecast residuals. Scenario demand is defined as

$$D_{s,t}^{\omega} = \hat{D}_{s,t}\left(1+\xi_{s,t}^{\omega}\right), \qquad \omega \in \Omega, \tag{40}$$

where $\xi_{s,t}^{\omega}$ denotes a sampled relative forecast error.

Only residuals from the model-fit period are used for scenario construction. Test residuals are excluded.

Ev, optimization, and computational parameters

Representative EV classes and battery parameters are adopted from Table 1. The efficiencies are set to

$$\eta^{\text{ch}} = 0.95, \qquad \eta^{\text{dis}} = 0.95. \tag{41}$$

The initial SoC is set to 60%. The operational SoC range is set to [20%, 90%] [43].

The adopted penalty values are

$$\lambda_{\text{volt}} = 500, \quad \lambda_{\text{thermal}} = 400, \quad \lambda_{\text{tr}} = 600, \quad \kappa = 50. \tag{42}$$

The penalty terms reduce constraint violations but do not guarantee that all original limits are satisfied in every interval. After MIQP refinement, each time interval is evaluated against the original voltage, line, transformer, and SoC constraints without penalty relaxation. A time interval is classified as feasible only when all of these limits are satisfied. The feasible-slot rate is defined as the percentage of intervals that pass this final ex-post feasibility check. The binary resolutions are

$$B_p = 5, \qquad B_v = 5. \tag{43}$$

The binary-grid error and feasibility checks are reported in Appendix "QUBO Formulation".

The binary-grid error is evaluated separately from the error caused by the approximate QUBO search.

Continuous refinement is performed by Gurobi 10.0 MIQP.

For MIQP, `MIPGap` = 1% and `TimeLimit` = 600 s are used. A solver time limit of 600 s is applied to both MIQP and the classical QUBO workflow. The reported end-to-end runtime includes model construction, optimization, solution recovery, final feasibility verification, and, for the classical QUBO workflow, MIQP refinement. Consequently, the reported end-to-end runtime may exceed the 600 s solver limit.

All data preparation, forecast, and optimization routines are implemented in Python 3.11. The `pandas` and `scikit-learn` packages are used. A custom LinDistFlow solver is used. QUBO construction and classical optimization are implemented with the D-Wave Ocean SDK.

Both methods are tested on the same workstation with an Intel Core i9-12900 K CPU, 128 GB RAM, and Ubuntu 22.04 LTS. An NVIDIA GeForce RTX 3090 GPU with 24 GB memory is installed, but GPU acceleration is not used for the reported optimization results.

Large-scale instances with $q \sim 10^4$ are solved by classical decomposition heuristics. The same decomposition rule and termination criterion are applied to all 30 daily instances. A fixed random seed of 42 is used for all QUBO runs.

Reduced cases with $q \leq 300$ are submitted to D-Wave Advantage through the same SDK. The Pegasus P16 topology is used. Minor embedding is obtained with `minorminer`. A total of 1000 reads and an anneal time of 20 μs are used for each case. Automatic coefficient scaling is enabled. The chain strength is set to 1.5 times the largest absolute QUBO coefficient. Broken chains are resolved by majority vote. The lowest-energy feasible sample is retained. QPU access time is obtained from the returned solver metadata. Queue time is excluded. These reduced cases are used only for binary compatibility tests. All reported large-scale results are obtained through classical computation.

Three baseline methods are defined. The first baseline is fixed ToU pricing. The second baseline is dynamic pricing without network constraints. The third baseline is deterministic optimization without uncertainty. For the MIQP-versus-classical-QUBO comparison, the same 30 daily instances, demand scenarios, objective function, and original LinDistFlow and SoC feasibility criteria are used for both methods. The results are reported as mean ± standard deviation.

Results

An evaluation of the proposed elasticity-aware menu pricing method is presented with the Jeju Island Plus DR EV Charging Dataset [11] and KEPCO ToU procurement tariffs [44]. Because feeder GIS, telemetry, and actual station connectivity data are not publicly available, the Jeju station profiles are assigned to the KADTS benchmark feeder [12] through the surrogate rule described in Section "Experimental setup". All voltage, line-load, transformer-load, and feeder-loss values are obtained from the LinDistFlow approximation introduced in Section "PDN-Constrained pricing and QUBO formulation". These values are reported as benchmark-based estimates. They are not presented as measurements from the actual Jeju distribution network.

Behavioral model estimation and forecasting accuracy

The multinomial logit demand model was calibrated through maximum likelihood estimation on the training set. Table 2 reports the estimated elasticity parameters for the user classes considered in this study. All coefficients have the expected signs, with commercial fleet

Table 2
Estimated MNL demand parameters (maximum likelihood estimation).

User class	α	Std.Err	β	Std.Err	δ	Std.Err
Fast charger commuter	1.42	0.12	0.018	0.004	0.63	0.08
Slow charger commuter	0.95	0.10	0.015	0.003	0.54	0.07
Commercial fleet	1.78	0.15	0.022	0.005	0.71	0.09
Occasional user	0.68	0.09	0.012	0.003	0.41	0.06

Table 3
Behavioral model estimation and validation results.

Metric	Training	Holdout
Log-likelihood	−2143.6	–
McFadden pseudo-R^2	0.221	–
RMSE (kW)	7.4	8.6
MAE (kW)	5.1	6.0
MAPE (%)	11.8	13.6

Table 4
Demand forecast performance on the Jeju EV dataset.

Method	MAPE (%)	RMSE (kW)
Persistence	12.45	58.21
RFR	8.36	39.82
GBR	**7.64**	**35.47**

users showing the highest price sensitivity and occasional users the lowest.

The MNL parameters are estimated only from October 2021 to June 2022 and are kept fixed during the July–December 2022 holdout test. No holdout observations are used for parameter estimation or model selection. With fixed elasticity parameters, holdout RMSE, MAE, and MAPE are 8.6 kW, 6.0 kW, and 13.6%, compared with training values of 7.4 kW, 5.1 kW, and 11.8%, respectively. The corresponding increases are 16.2%, 17.6%, and 15.3%, which support the temporal transferability of the estimated elasticity parameters.

Table 3 summarizes model fit and holdout validation performance, indicating that the aggregate behavioral model captures charging demand response with acceptable accuracy for tariff optimization.

Forecast accuracy is assessed on the chronological test period using MAPE and RMSE. As reported in Table 4, both tree-based models outperform the persistence benchmark. RFR reduces MAPE from 12.45% to 8.36% and RMSE from 58.21 to 39.82 kW. GBR provides the best performance, with a MAPE of 7.64% and an RMSE of 35.47 kW, and is therefore used to generate the demand forecasts provided to the optimization model.

A persistence forecast is used as the benchmark:

$$\hat{D}^{\text{pers}}_{s,t} = D_{s,t-1}. \tag{44}$$

Distribution network feasibility and reliability

We compare three pricing strategies: flat pricing, dynamic pricing without PDN coupling, and the proposed Q-MENU-PDN. Table 5 summarizes the resulting physical network metrics over the test horizon. Flat pricing and dynamic pricing without PDN coupling do not enforce network constraints. Their maximum line loadings of 121.4% and 108.6%, respectively, therefore represent thermal overloads in the adopted KADTS feeder. The comparison is intended to quantify the value of network-aware pricing rather than to compare equally feasible strategies. Q-MENU-PDN accounts for voltage, line, transformer, and SoC limits through the penalized optimization and subsequent MIQP refinement. After refinement, each interval is checked against the original constraints. The maximum line loading is limited to 94.3%, the maximum voltage deviation is reduced to 0.025 p.u., and the transformer peak loading is reduced to 91.5%. Overall, 96.3% of the intervals satisfy all original voltage, line, transformer, and SoC limits.

Table 5
Physical distribution network performance metrics (LinDistFlow-based).

Metric	Flat	Dynamic (no PDN)	Q-MENU-PDN
Max voltage deviation (p.u.)	0.046	0.039	**0.025**
Avg voltage deviation (p.u.)	0.021	0.018	**0.012**
Max line loading (%)	121.4	108.6	**94.3**
Transformer peak loading (%)	117.2	104.8	**91.5**
Average real power losses (kW)	184.2	171.5	**158.7**
Feasible time slots satisfying all limits (%)	68.4	82.1	**96.3**

A time slot is classified as feasible only when the original voltage, line, transformer, and SoC limits are simultaneously satisfied.

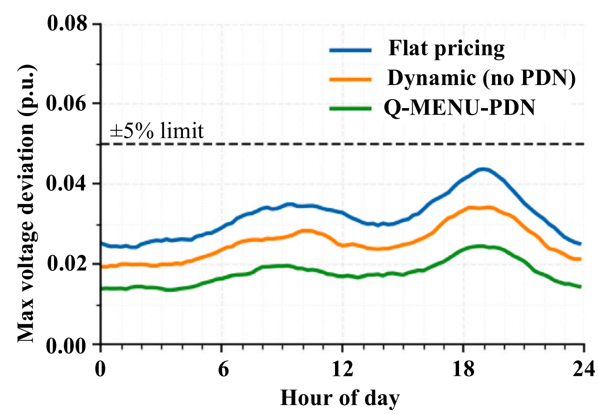

Fig. 2. Maximum feeder voltage deviation over 24 h under three pricing strategies.

The remaining 3.7% contain at least one residual violation. Therefore, the proposed procedure substantially improves feasibility but does not guarantee complete all-interval feasibility.

Relative to flat pricing, average real power losses decrease from 184.2 kW to 158.7 kW. Fig. 2 confirm that network-aware pricing suppresses evening voltage stress and mitigates localized thermal congestion without shifting overloads elsewhere in the feeder.

A re-optimized network-rating sensitivity analysis is performed by jointly scaling all line and transformer ratings by $\kappa_{\text{net}} \in \{0.9, 1.0, 1.1\}$. The optimization is repeated for each rating scale using the same demand scenarios and model settings, while the menu-pricing and dispatch decisions are recalculated under the modified network limits. As reported in Table 6, reducing the ratings by 10% ($\kappa_{\text{net}} = 0.9$) increases maximum line loading from 94.3% to 99.8%, decreases the feasible-slot rate from 96.3% to 91.7%, and reduces social welfare from 30.10 to 29.32 MKRW. Conversely, increasing the ratings by 10% ($\kappa_{\text{net}} = 1.1$) reduces maximum line loading to 89.1%, increases the feasible-slot rate to 98.5%, and raises social welfare to 30.42 MKRW. These results show that stricter network ratings reduce both operational feasibility and economic performance, whereas additional network capacity improves both outcomes.

Battery-constrained V2G impacts

Table 7 compares Q-MENU-PDN with and without SoC-feasible V2G dispatch. Under full nominal class-level availability, 3.2 MWh of V2G energy is obtained, and the peak net load is reduced by 250.0 kW. The 3.2 MWh value is treated as a nominal upper estimate and not as an expected field value. Maximum line load is reduced from 97.6%

Table 6
Re-optimized sensitivity to joint line and transformer rating variation.

κ_{net}	Social welfare (MKRW)	Feasible time slots (%)	Maximum line loading (%)
0.9	29.32	91.7	99.8
1.0	30.10	96.3	94.3
1.1	30.42	98.5	89.1

Table 7
Impact of battery-constrained V2G under LinDistFlow feasibility.

Metric	Without V2G	With V2G
Dispatchable V2G energy (MWh)	0.0	**3.2**
Peak net load reduction (kW)	0.0	**250.0**
Max line loading (%)	97.6	**94.3**
Max voltage deviation (p.u.)	0.029	**0.025**
Transformer peak loading (%)	94.2	**91.5**
Average real power losses (kW)	163.9	**158.7**
Social welfare (MKRW)	29.42	**30.10**

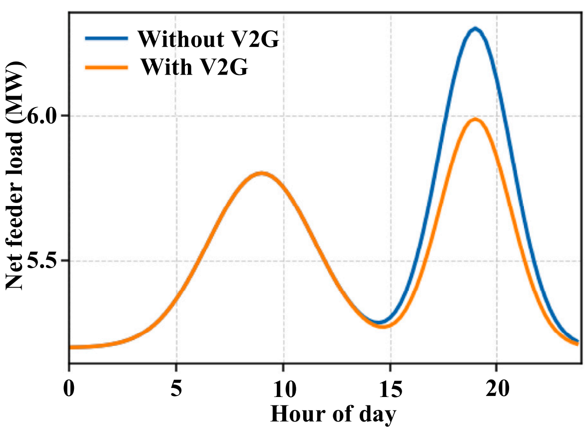

Fig. 3. Peak-day feeder net load with and without SoC-feasible V2G.

to 94.3%, transformer peak load is reduced from 94.2% to 91.5%, and average real power losses are reduced from 163.9 kW to 158.7 kW. Social welfare increases from 29.42 to 30.10 MKRW. The V2G benefit is therefore attributed mainly to feasible peak reduction rather than energy arbitrage alone. Fig. 3 shows the related reduction in peak-day feeder load.

Optimization performance and computational efficiency

We compare the hybrid QUBO–classical workflow with a classical MIQP baseline under identical LinDistFlow constraints and demand realizations. All full-scale results are obtained using classical computation; reduced quantum runs are used only for validation-scale embedding tests.

For each daily instance r, the best feasible objective obtained by either method within the common 600 s solver-time limit is used as the reference.

$$J^r_{a,\text{best}}(t) = \max_{\substack{0\le\tau\le t \\ \text{solution feasible at } \tau}} J^r_a(\tau). \tag{45}$$

The best feasible objective obtained by either method within the common 600 s solver limit is then used as the reference:

$$J^r_{\text{ref}} = \max_a J^r_{a,\text{best}}(600). \tag{46}$$

The common-reference gap for method a at time t is defined as

$$g^r_a(t) = \frac{J^r_{\text{ref}} - J^r_{a,\text{best}}(t)}{\left|J^r_{\text{ref}}\right|} \times 100\%. \tag{47}$$

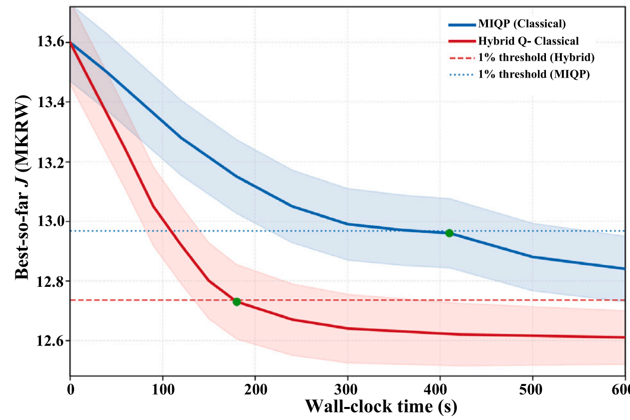

Fig. 4. Mean best-so-far feasible objective trajectories over 30 daily instances under identical LinDistFlow and SoC constraints. For each method, the best-so-far objective at time t is the maximum feasible objective obtained up to that time. Shaded regions indicate ± 1 standard deviation.

Only solutions satisfying the original LinDistFlow and SoC constraints are included in the best-so-far sequence. The same reference is used for both methods within each daily instance. The reported objective trajectory and common-reference gap are averaged over the 30 daily instances.

Fig. 4 shows that the hybrid workflow reaches a mean common-reference gap below 1% after approximately 180 s, whereas MIQP reaches the same threshold after approximately 410 s. As summarized in Table 8, the hybrid method reduces the mean end-to-end runtime from 612.3 $\pm$ 74.5 s to 298.4 $\pm$ 36.7 s. At a solver time of 300 s, it achieves a smaller mean common-reference gap than MIQP (0.9% versus 3.8%). The final mean objective values are 12.61 $\pm$ 0.09 MKRW for the hybrid method and 12.84 $\pm$ 0.11 MKRW for MIQP. The difference between these two final mean objective values is 1.79%. This percentage is calculated from the reported mean objectives and is distinct from the per-instance common-reference gap. The maximum five-bit discretization error is 0.42%, as reported in Appendix "Discretization and feasibility check". Therefore, the final objective difference cannot be attributed to discretization alone; it also reflects the approximate QUBO search and decomposition procedure. These results demonstrate a trade-off between runtime and solution quality rather than a strict algorithmic speedup. Reported runtimes include model construction and final feasibility checks and may therefore exceed the 600 s solver limit.

Economic outcomes and welfare trade-offs

Table 9 reports operator revenue, user surplus, and social welfare for the MIQP-refined dispatch. Results are reported as mean $\pm$ standard deviation across runs. Q-MENU-PDN achieves the highest social welfare, increasing it from 26.68 MKRW under flat pricing and 27.60 MKRW under dynamic pricing without PDN coupling to 30.10 MKRW. The gain is driven primarily by higher user surplus, which increases from 12.47 to 15.74 MKRW, while operator revenue remains stable and slightly improves relative to both baselines. Fig. 5 shows the decomposition of welfare into operator revenue and user surplus, and Fig. 6 confirms that the welfare improvement is achieved together with a reduction in maximum line loading from 121.4% under flat pricing to 94.3% under Q-MENU-PDN.

Robustness and sensitivity analysis

Robustness is assessed under demand forecast error, V2G availability, EV-class composition, battery degradation cost, and network parameter variation.

Table 8
Computational performance over 30 daily instances under identical LinDistFlow and SoC feasibility criteria. Objective values and runtimes are reported as mean ± standard deviation, while percentage values are averaged over the 30 instances.

Method	J^* (MKRW)	End-to-end runtime (s)	Common-reference gap at 300 s (%)	Difference between final mean objectives (%)
MIQP (Classical)	12.84 ± 0.11	612.3 ± 74.5	3.8	0.00
Hybrid QUBO–Classical	12.61 ± 0.09	298.4 ± 36.7	0.9	1.79

Table 9
Economic outcomes over the test horizon.

Method	Rev (MKRW)	US (MKRW)	SW (MKRW)
Flat pricing	14.21 ± 0.08	12.47 ± 0.10	26.68 ± 0.12
Dynamic pricing (no PDN)	14.08 ± 0.07	13.52 ± 0.09	27.60 ± 0.11
Q-MENU-PDN	**14.36 ± 0.06**	**15.74 ± 0.08**	**30.10 ± 0.10**

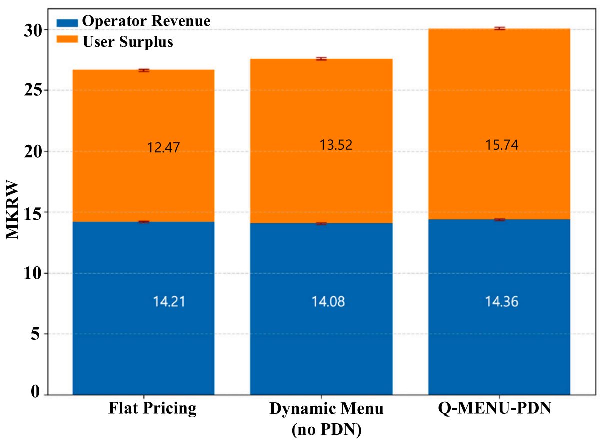

Fig. 5. Breakdown of social welfare into operator revenue and user surplus after MIQP refinement.

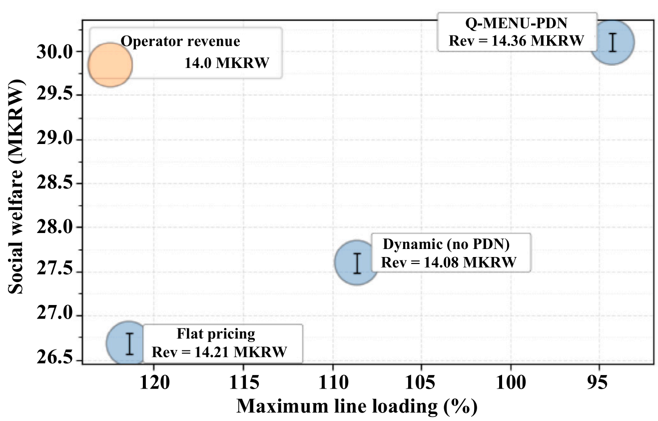

Fig. 6. Trade-off between SW and maximum line loading under the three pricing strategies. Bubble area denotes operator revenue, with a 14.0 MKRW reference marker and exact revenue annotations.

The LinDistFlow model is adopted. It is shown in Table 10 that a 20% forecast error raises maximum line loading to 105.9% and reduces SW to 28.71 MKRW. However, SW is retained above the flat-pricing value.

For the availability test, a uniform scale η is applied to the effective availability factor:

$$a_{s,t}^{c} = \eta, \qquad \forall s, t, c. \tag{48}$$

The scale represents vehicle presence, station occupancy, and user consent. The value $\eta = 1.0$ denotes full nominal availability. The value

Table 10
Impact of demand forecast uncertainty on physical feasibility (Q-MENU-PDN).

Forecast error	Max line loading (%)	Max voltage Dev. (p.u.)	SW (MKRW)
0%	94.3	0.025	30.10
10%	98.7	0.028	29.64
20%	105.9	0.034	28.71

Table 11
Sensitivity to effective V2G availability.

η	V2G energy (MWh)	Max line loading (%)	Losses (kW)	SW (MKRW)
1.0	3.2	94.3	158.7	30.10
0.6	1.9	96.8	160.9	29.73
0.3	1.0	99.5	162.4	29.21

$\eta = 0.6$ denotes moderate restrictions. The value $\eta = 0.3$ denotes severe restrictions. Nominal V2G energy is scaled in direct proportion to η.

At $\eta = 0.3$, nominal V2G energy decreases from 3.2 to 1.0 MWh. Maximum line loading increases from 94.3% to 99.5%. Feeder losses increase from 158.7 to 162.4 kW. SW decreases from 30.10 to 29.21 MKRW, which corresponds to a reduction of approximately 3.0%. The thermal limit is still satisfied. SW is also retained above the flat-pricing value.

Sensitivity to EV-class composition is also assessed. Three class-weight cases are defined. The light-fleet case assigns larger shares to compact BEV and sedan BEV classes. The South Korean base case uses the weights reported in Table 1. The heavy-fleet case assigns a larger share to the SUV BEV class. In each case, $\sum_{c\in C} \rho_c = 1$.

The midpoint battery capacity of class c is denoted by $\bar{E}_c = (E_c^{\min} + E_c^{\max})/2$. The weighted battery capacity is defined as

$$\bar{E}_\rho = \sum_{c\in C} \rho_c \bar{E}_c. \tag{49}$$

The class-composition scale is defined relative to the South Korean base case:

$$\kappa_\rho = \frac{\bar{E}_\rho}{69.75}. \tag{50}$$

The resulting scales are 0.934, 1.000, and 1.052 for the light-fleet, South Korean base, and heavy-fleet cases, respectively. The corresponding V2G energy, SW, and line-load values are obtained by linear interpolation of the V2G-capability results in Table 14. This ex-post test isolates the effect of class composition. A new optimization run is not claimed.

A limited effect from the assessed class-weight changes is shown in Table 12. V2G energy varies from 3.0 to 3.4 MWh. SW varies from 29.98 to 30.19 MKRW. Maximum line loading varies from 94.6% to 94.1%. The economic and feeder result order is retained across the three cases.

The South Korean class weights are treated as the base case. They are not assumed to represent all EV markets. Application to another market requires local class shares, battery capacities, charge limits, discharge limits, and V2G rules. The mathematical formulation remains unchanged after these parameters are replaced.

A throughput-based battery degradation cost is also assessed [45, 46]. The cost is defined as

$$C^{\mathrm{deg}} = 10^{-6} \sum_{s,t,c} c_c^{\mathrm{deg}} P_{s,t}^{\mathrm{dis},c} \Delta t. \tag{51}$$

Table 12
EV-class composition cases and corresponding ex-post sensitivity results.

Case	Compact	Crossover	Sedan	SUV	$\bar{E}_\rho$ (kWh)	κ_ρ	V2G energy (MWh)	SW (MKRW)	Max line load (%)
Light-fleet case	0.35	0.30	0.20	0.15	65.13	0.934	3.0	29.98	94.6
South Korean base case	0.20	0.35	0.15	0.30	69.75	1.000	3.2	30.10	94.3
Heavy-fleet case	0.10	0.30	0.10	0.50	73.35	1.052	3.4	30.19	94.1

Table 13
Ex-post sensitivity under fixed nominal decisions.

Panel A: Battery degradation cost under fixed nominal V2G dispatch

Case	c^{deg} (KRW/kWh)	V2G energy (MWh)	SW^{deg} (MKRW)	Max line load (%)
Low	5	3.2	30.08	94.3
Medium	50	3.2	29.94	94.3
High	125	3.2	29.70	94.3

Panel B: Line thermal-rating reduction under fixed nominal pricing and dispatch decisions

Line-rating scale κ_{line}	Feasible slots (%)	Max. line loading (%)	SW (MKRW)
1.0	96.3	94.3	30.10
0.9	89.4	104.7	29.02
0.8	76.8	118.9	27.84

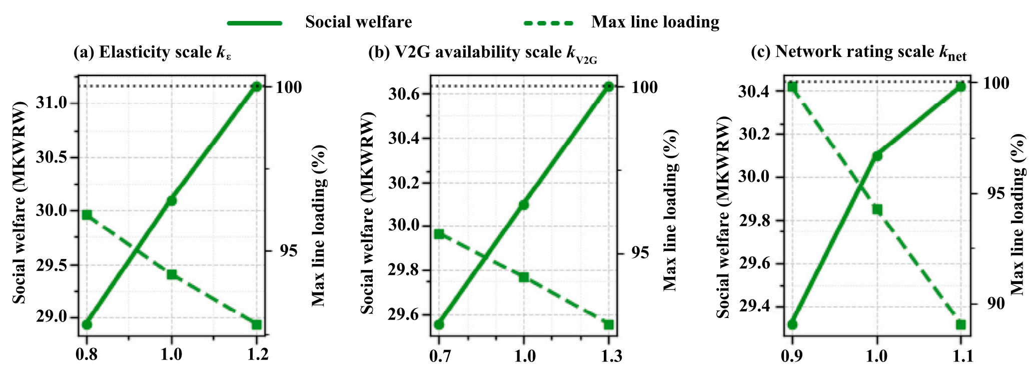

Fig. 7. Sensitivity of SW and maximum line loading to parameter scales under Q-MENU-PDN. Solid lines refer to SW and the left axis, whereas dashed lines refer to maximum line loading and the right axis. Panel (a) presents the elasticity scale κ_ϵ. Panel (b) presents the technical V2G discharge-capability scale κ_{V2G}. Panel (c) presents the re-optimized joint line-and-transformer rating scale κ_{net}. The 100% thermal threshold is marked by the dotted horizontal line.

The value c_c^{deg} is expressed in KRW/kWh, and C^{deg} is expressed in MKRW. Degradation-adjusted SW is defined as

$$SW^{\text{deg}} = SW - C^{\text{deg}}. \tag{52}$$

The throughput-cost form is supported by Refs. [45,46]. Three assumed cost levels are tested. The values are not presented as direct estimates from the cited studies or as fixed South Korean market values. The nominal V2G dispatch is retained so that the direct economic effect is isolated. The results are reported in Panel A of Table 13.

A separate ex-post line-rating stress test is presented in Panel B of Table 13. Unlike the re-optimized joint network-rating analysis in Table 6, the nominal pricing and dispatch decisions are retained, and only the line thermal ratings are reduced. Consequently, a 10% line-rating reduction increases the maximum line loading from 94.3% to 104.7%. By contrast, re-optimization under jointly reduced line and transformer ratings limits the maximum line loading to 99.8%. Lower line ratings also reduce the feasible-slot rate and social welfare. At line-rating scales of 0.9 and 0.8, the thermal limit is exceeded; however, social welfare remains above the flat-pricing value in both cases.

Further parameter sensitivity results are reported in Fig. 7, Table 6, and Table 14. SW is increased and feeder stress is reduced by higher elasticity and V2G discharge capability. The feasible-slot rate and SW are increased by less restrictive network ratings. The maximum line load is also reduced.

Even at $\kappa_\epsilon = 0.8$, SW remains 28.94 MKRW, which is 8.5% above the flat-pricing value of 26.68 MKRW. Thus, the economic advantage over flat pricing is retained under the assessed reduction in demand elasticity.

Unlike the availability analysis in Table 11, which represents vehicle presence, station occupancy, and user consent, the sensitivity test in Panel B of Table 14 is based on a change in the technical V2G discharge-capability limit.

Discussion

The results show that Q–MENU–PDN improves feeder reliability and economic performance. The proposed method combines demand forecasting, PDN-aware menu pricing, and SoC-feasible V2G dispatch within a unified optimization framework. Across the test horizon, maximum line loading is limited to 94.3%, maximum voltage deviation to 0.025 p.u., and average real power losses to 158.7 kW, while social welfare reaches 30.10 MKRW.

Under the adopted KADTS benchmark and LinDistFlow assumptions, these results indicate that congestion-aware pricing can improve economic efficiency while reducing feeder stress.

Forecasting and PDN-aware pricing

The results show that demand estimation is important for network-aware pricing. The proposed forecasting method reduces MAPE from 12.45% to 7.64% and RMSE from 58.21 kW to 35.47 kW. This supports more reliable tariff decisions under temporal EV charging variation. Sensitivity results also show that stronger calibrated elasticity improves welfare and reduces feeder stress. Therefore, elasticity calibration is not only an economic modeling step. It is also an important factor for physical grid reliability under menu-based pricing.

Table 14
Sensitivity to demand elasticity and V2G discharge-capability scales under Q-MENU-PDN, LinDistFlow, and SoC-feasible V2G.

Panel A: Demand elasticity scale

κ_ϵ	SW (MKRW)	Max. voltage dev. (p.u.)	Max. line load (%)
0.8	28.94	0.028	96.1
1.0	30.10	0.025	94.3
1.2	**31.16**	**0.023**	**92.8**

Panel B: V2G discharge-capability scale

κ_{V2G}	V2G energy (MWh)	SW (MKRW)	Max. line load (%)	Max. voltage dev. (p.u.)
0.7	2.2	29.56	95.6	0.027
1.0	3.2	30.10	94.3	0.025
1.3	**4.1**	**30.63**	**92.9**	**0.023**

Classical QUBO solution and reduced D-wave test

The QUBO is used as a classical combinatorial representation for all full-scale cases. Classical decomposition is first applied. MIQP refinement is then applied to improve feasibility and the objective value. D-Wave hardware is used only for reduced cases with $q \leq 300$ to verify binary encoding and minor-embedding compatibility. No full-scale quantum result or hardware-based quantum speedup is reported.

Economic and welfare implications

Q-MENU-PDN improves social welfare and increases the rate of feasible network intervals. Social welfare increases from 26.68 MKRW under flat pricing and 27.60 MKRW under dynamic pricing without PDN coupling to 30.10 MKRW. User surplus increases from 12.47 to 15.74 MKRW, while operator revenue remains stable. This result shows that the welfare gain is mainly obtained from better user benefit and feeder-aware allocation, not from aggressive tariff extraction. Battery-constrained V2G further supports this result. It provides 3.2 MWh of dispatchable energy and reduces peak net load by 250.0 kW.

Robustness and deployment context

Sensitivity to demand forecast error, V2G availability, and network ratings is assessed. Under severe forecast error, a higher line load and lower welfare are observed. Under lower V2G availability, the peak-load benefit is reduced. However, an economic advantage over flat pricing is retained. Under lower network ratings, fewer feasible intervals and lower welfare are obtained. These tests are limited to the adopted KADTS topology, the surrogate station-to-node assignment, and the LinDistFlow approximation. Uncertainty from the station-to-node assignment is not removed by these tests. The reported voltage and thermal values are therefore interpreted only within the adopted benchmark. Direct representation of the actual Jeju feeder is not claimed. A complete UTN–PDN model is also not claimed. The method can support an initial assessment of congestion-aware EV tariffs when actual feeder data are unavailable. Direct operator use requires feeder GIS, station connectivity, network telemetry, and a higher-fidelity AC validation.

Carbon and consumer-side implications

The reduction in peak net load and feeder losses suggests that the proposed method can support carbon reduction when marginal peak supply is fossil-based. The method can also support practical EV charging operation. EV chargers can receive price signals, select charging or V2G actions within SoC limits, and return state information to the operator. This reduces the need for direct centralized control of every individual battery.

Limitations and future work

Several limitations should be noted. First, the V2G model is based on class-level battery parameters rather than vehicle-level mobility trajectories. Stochastic arrival and departure behavior, travel uncertainty, and battery degradation costs are not represented explicitly.

The reported 3.2 MWh is therefore treated as a nominal upper estimate rather than an expected field value.

Second, network operation is represented by LinDistFlow. Full AC nonlinearities, phase imbalance, and reactive power effects are not represented. Third, infrastructure ratings are fixed within each scenario. Ambient effects, contingencies, and dynamic equipment limits are not represented explicitly. Finally, classical QUBO decomposition is used for realistic problem sizes because current NISQ-era hardware cannot solve the full-scale formulation directly. Tariff bounds and V2G credits are based on the adopted KEPCO case. Regulatory approval, settlement rules, and market participation limits are not represented. User consent is represented only through the availability factor. Actual user acceptance can therefore be lower. Aggregate behavioral data are used, but privacy risks from record linkage and reidentification are not assessed. The station-to-feeder association is used as a surrogate, and its uncertainty is not quantified. Direct deployment is therefore restricted. Future work is directed toward stochastic mobility-aware and degradation-aware V2G models, higher-fidelity AC network models, probabilistic grid-constrained tariffs, adaptive elasticity estimation, privacy safeguards, and scalable quantum–classical solution methods.

Conclusion

Q–MENU–PDN is presented as a QUBO-based EV menu pricing method. Elasticity-aware demand, SoC-feasible V2G dispatch, and LinDistFlow constraints are represented in one optimization model. The Jeju Island DR profiles are assigned to the KADTS benchmark feeder through a surrogate station-to-node rule. Therefore, the demand assessment is empirically based, while the network assessment is benchmark-based. Relative to flat pricing and PDN-agnostic pricing, better economic and feeder outcomes are obtained under the adopted assumptions. Maximum line loading is reduced to 94.3%, maximum voltage deviation is limited to 0.025 p.u., and average feeder losses are reduced to 158.7 kW. A dispatchable V2G energy of 3.2 MWh is obtained, and a peak net-load reduction of approximately 250 kW is achieved. Social welfare is increased from 26.68 to 30.10 MKRW, which represents a 12.8% increase. Mean runtime is reduced from 612 s to 298 s relative to the classical MIQP baseline. The reported network values apply to the KADTS assignment and the LinDistFlow assumptions. They do not represent measurements from the actual Jeju feeder. No complete UTN model is included, and no comprehensive UTN–PDN coupling claim is made. Direct deployment requires actual feeder connectivity, GIS data, network telemetry, and full AC validation.

CRediT authorship contribution statement

Lilia Tightiz: Writing – review & editing, Writing – original draft, Visualization, Validation, Supervision, Methodology, Investigation, Conceptualization. **L. Minh Dang:** Writing – review & editing, Methodology, Investigation, Conceptualization. **Hyosik Yang:** Writing – review & editing, Supervision, Methodology, Funding acquisition, Conceptualization.

Declaration of competing interest

The authors declare that they have no known competing financial interests or personal relationships that could have appeared to influence the work reported in this paper.

Acknowledgments

This research was supported by the "Korea Electric Power Corporation" (R25XO03-16).

Appendix A. QUBO reformulation

This appendix summarizes the conversion of the elasticity-aware EV pricing problem with LinDistFlow constraints into QUBO form.

Appendix A.1. Binary encoding

Continuous variables are discretized through binary expansion. For each station s, time interval t, and menu option m, charging prices are written as

$$p_{s,t}^{m} = p_{\min} + \Delta_p \sum_{\ell=0}^{b_p-1} 2^{\ell} x_{s,t,m,\ell}, \qquad x_{s,t,m,\ell} \in \{0,1\}, \tag{A.1}$$

and V2G credits are written as

$$v_{s,t}^{m} = v_{\min} + \Delta_v \sum_{\ell=0}^{b_v-1} 2^{\ell} y_{s,t,m,\ell}. \tag{A.2}$$

All binary variables are collected into $\mathbf{z} \in \{0,1\}^q$.

Appendix A.2. Compact PDN and battery constraints

The principal PDN limits are represented through the LinDistFlow constraints:

$$\mathcal{F}_{\mathrm{PDN}} = \left\{ P_{ij,t}, Q_{ij,t}, V_{n,t} : \begin{array}{c} V_{\min} \le V_{n,t} \le V_{\max}, \\ P_{ij,t}^2 + Q_{ij,t}^2 \le \left(S_{ij}^{\max}\right)^2, \\ P_{\mathrm{root},t}^2 + Q_{\mathrm{root},t}^2 \le \left(S_{\mathrm{tr}}^{\max}\right)^2 \end{array} \right\}. \tag{A.3}$$

Aggregated SoC dynamics for EV class c are written as

$$\mathrm{SoC}_{s,t+1}^{c} = \mathrm{SoC}_{s,t}^{c} + \eta_c^{\mathrm{ch}} \frac{P_{s,t}^{\mathrm{ch},c} \Delta t}{N_{s,t}^{c} E_c^{\max}} - \frac{1}{\eta_c^{\mathrm{dis}}} \frac{P_{s,t}^{\mathrm{dis},c} \Delta t}{N_{s,t}^{c} E_c^{\max}}, \qquad N_{s,t}^{c} > 0. \tag{A.4}$$

When $N_{s,t}^{c} = 0$, both $P_{s,t}^{\mathrm{ch},c}$ and $P_{s,t}^{\mathrm{dis},c}$ are set to zero.

Appendix A.3. Quadratic demand approximation

The systematic utility of menu option m for behavioral class $h(s)$ is defined as

$$V_{s,t}^{m,h(s)} = -\alpha_{h(s)} p_{s,t}^{m} + \beta_{h(s)} v_{s,t}^{m} - \delta_{h(s)} \Delta\tau_{s,t}^{m}. \tag{A.5}$$

The MNL choice probability is defined as

$$\pi_{s,t}^{m,h(s)} = \frac{\exp\left(V_{s,t}^{m,h(s)}\right)}{\sum_{\ell=1}^{K} \exp\left(V_{s,t}^{\ell,h(s)}\right)}. \tag{A.6}$$

Table A.15
Binary-grid resolution relative to each variable range.

B	Levels	$\Delta p_B/(p^{\max}-p^{\min})$	$\Delta v_B/(v^{\max}-v^{\min})$	Max half-step
4	16	6.67%	6.67%	3.33%
5	32	3.23%	3.23%	1.61%
6	64	1.59%	1.59%	0.79%

For concise notation, the behavioral-class index is omitted below, and $\pi_{s,t}^{m}$ denotes $\pi_{s,t}^{m,h(s)}$. The menu demand under scenario ω is defined as

$$d_{s,t}^{m,\omega} = \pi_{s,t}^{m} D_{s,t}^{\omega}. \tag{A.7}$$

For each (s,t,m,ω), a second-order approximation is used for the QUBO representation:

$$\widetilde{d}_{s,t}^{m,\omega}(\mathbf{z}) = c_0 + \sum_i c_i z_i + \sum_{i<j} c_{ij} z_i z_j. \tag{A.8}$$

Appendix A.4. QUBO formulation

The optimization problem is written as

$$\min_{\mathbf{z}\in\{0,1\}^q} \mathbf{z}^{\top} Q \mathbf{z}, \tag{A.9}$$

where

$$Q = Q_{\mathrm{econ}} + \lambda_{\mathrm{thermal}} Q_{\mathrm{thermal}} + \lambda_{\mathrm{volt}} Q_{\mathrm{volt}} + \lambda_{\mathrm{tr}} Q_{\mathrm{tr}} + \kappa Q_{\mathrm{risk}}. \tag{A.10}$$

The term Q_{econ} is obtained from $-\widehat{J}(\mathbf{z})$, where $\widehat{J}(\mathbf{z})$ denotes the quadratic approximation of the economic maximization objective. Therefore, minimization of the QUBO energy corresponds to maximization of the approximated economic objective before the penalty terms are added.

Appendix A.5. Discretization and feasibility check

Let J_{cont}^{r} denote the objective value from the continuous MIQP for daily instance r. Let J_{disc}^{r} denote the value from the same model after the price and credit variables are restricted to the binary grid. The discretization error is defined as

$$e_{\mathrm{disc}}^{r} = \frac{\left|J_{\mathrm{cont}}^{r} - J_{\mathrm{disc}}^{r}\right|}{\left|J_{\mathrm{cont}}^{r}\right|} \times 100\%. \tag{A.11}$$

For a resolution of B bits, the price and credit steps are (see Table A.15).

$$\Delta p_B = \frac{p^{\max} - p^{\min}}{2^B - 1}, \qquad \Delta v_B = \frac{v^{\max} - v^{\min}}{2^B - 1}. \tag{A.12}$$

The five-bit case provides 32 values for each price and credit variable. The maximum objective error across the 30 daily instances is 0.42%. This resolution is retained as a compromise between binary size and objective accuracy.

Appendix B. Station-to-feeder assignment details

The numerical inputs for the surrogate assignment are reported in Table B.16.

The assignment procedure is specified below.

1. The retained station set is formed from Eq. (28).
2. The interval-average demand is calculated from Eq. (29).
3. The station peak is calculated from Eq. (30).
4. The stations are ordered by decreasing station peak. Equal peak values are ordered by ascending customer ID.
5. The node weights are set from Eq. (33).
6. The station quotas are set from Eq. (35).
7. The initial cumulative peak is set to zero for each node.

Table B.16
Reference loads, node weights, and station quotas.

KADTS node	Reference load (MW)	Node weight	Assigned stations
3	25	0.25	134
4	25	0.25	134
16	10	0.10	54
22	10	0.10	53
34	10	0.10	53
43	10	0.10	53
53	10	0.10	53
Total	100	1.00	534

Table C.17
Adopted forecast parameters.

Method	Parameter	Adopted value
GBR	`n_estimators`	300
GBR	`learning_rate`	0.03
GBR	`max_depth`	3
GBR	`subsample`	0.80
GBR	`min_samples_leaf`	5
GBR	`random_state`	42
RFR	`n_estimators`	500
RFR	`max_depth`	20
RFR	`max_features`	`sqrt`
RFR	`min_samples_leaf`	2
RFR	`bootstrap`	`True`
RFR	`random_state`	42

8. Each station is assigned by Eq. (38).
9. A tie is resolved by the lowest node number.
10. The cumulative node peak and station count are updated after each assignment.
11. The final association is fixed for the full test period.

The procedure does not use station coordinates, geographic distance, charger type, road data, traffic data, route choice, feeder GIS, or actual station connectivity. The procedure does not contain an explicit UTN optimization model. The assignment provides a reproducible surrogate association between empirical station demand and the KADTS benchmark nodes.

Appendix C. Forecast model details

The forecast parameters are selected by five-fold sequential-origin validation. Mean validation RMSE is used as the selection criterion. A fixed seed of 42 is used for both methods. The adopted values are reported in Table C.17.

GBR is selected because the lowest mean validation RMSE is obtained. RFR is retained as a tree-based comparator. The final GBR model is fitted with the full model-fit period. The chronological test period is used only for final performance assessment.

Data availability

Data will be made available on request.

References

[1] Tightiz L, Dang LM, Yoo J J, Padmanaban S. A comprehensive review on AIoT applications for intelligent EV charging/discharging ecosystem. Energy Convers Manag: X 2025;10:101088.
[2] He B, Yang B, Han Y, Zhou Y, Hu Y, Shu H, Su S, Yang J, Huang Y, Li J, Jiang L. Optimal EVCS planning via spatial–temporal distribution of charging demand forecasting and traffic-grid coupling. Energy 2024;313:133885.
[3] Limmer S. Dynamic pricing for electric vehicle charging—a literature review. Energies 2019;12(18):3574.
[4] Cui L, Wang Q, Qu H, Wang M, Wu Y, Ge L. Dynamic pricing for fast charging stations with deep reinforcement learning. Appl Energy 2023;346:121334.
[5] Lu C, Wu J, Cui J, Xu Y, Wu C, Gonzalez MC. Deadline differentiated dynamic EV charging price menu design. IEEE Trans Smart Grid 2023;14(1):502–16.
[6] Dupont A, Breal JB, Hayel Y, Andrianesis P. Optimal price menu design of electric vehicle charging stations providing demand response. Electr Power Syst Res 2024;235:110798.
[7] Telford R, Stephen B, Browell J, Haben S. Dirichlet sampled capacity and loss estimation for LV distribution networks with partial observability. IEEE Trans Power Deliv 2021;36(5):2676–86.
[8] Chen S, Cheng H, Zhang H, Lv S, Wei Z, Jin Y. Privacy-preserving coordination of power and transportation networks using spatiotemporal GAT for predicting EV charging demands. Appl Energy 2025;377:124391.
[9] Veshchezerova M, Somov M, Bertsche D, Limmer S, Schmitt S, Perelshtein M, Tripathi AJ. A hybrid quantum–classical approach to the electric mobility problem. In: IEEE international conference on quantum computing and engineering. QCE, Bellevue, WA, USA; 2023, p. 636–41.
[10] Tightiz L, Padmanaban S, Bang S, Yang HS. Quantum computing for big data optimization in decentralized smart grids: A comprehensive review of computation, security, and P2P energy transactions. TechRxiv 2025. http://dx.doi.org/10.36227/techrxiv.175393426.64156699/v1.
[11] Baek K, Lee J, Kim H. EV charging infrastructure demand response dataset: integrated operational and market data from Jeju Island. figshare; 2025, Dataset. Available: https://figshare.com/articles/dataset/EV_charging_infrastructure_demand_response_dataset_integrated_operational_and_market_data_from_Jeju_island/29617100.
[12] Ramadhan Maulana I, Zafar R, Chung I-Y. A bilevel optimization framework for hybrid DSO-VPP coordination: Enhancing congestion management and market efficiency in decentralized energy systems. IEEE Access 2025;13:153281–95.
[13] Dupont A, Breal JB, Hayel Y, Andrianesis P. Optimal price menu design of electric vehicle charging stations providing demand response. Electr Power Syst Res 2024;235:110798.
[14] Zhang Y, You P, Cai L. Optimal charging scheduling by pricing for EV charging station with dual charging modes. IEEE Trans Intell Transp Syst 2019;20(9):3386–96.
[15] Lai S, Qiu J, Tao Y, Zhao J. Pricing for electric vehicle charging stations based on the responsiveness of demand. IEEE Trans Smart Grid 2023;14(1):530–44.
[16] Kuang H, Qu H, Deng K, Li J. A physics-informed graph learning approach for citywide electric vehicle charging demand prediction and pricing. Appl Energy 2024;363:123059.
[17] Kim H, Kim DW, Kim MK. Economics of charging infrastructure for electric vehicles in Korea. Energy Policy 2022;164:112875.
[18] Luo C, Huang Y-F, Gupta V. Stochastic dynamic pricing for EV charging stations with renewable integration and energy storage. IEEE Trans Smart Grid 2018;9(2):1494–505.
[19] Kazemtarghi A, Mallik A, Chen Y. Dynamic pricing strategy for electric vehicle charging stations to distribute the congestion and maximize the revenue. Int J Electr Power Energy Syst 2024;158:109946.
[20] Cedillo MH, Sun H, Jiang J, Cao Y. Dynamic pricing and control for EV charging stations with solar generation. Appl Energy 2022;326:119920.
[21] Cui Y, Hu Z, Duan X. Optimal pricing of public electric vehicle charging stations considering operations of coupled transportation and power systems. IEEE Trans Smart Grid 2021;12(4):3278–88.
[22] Zhao Z, Lee CKM. Dynamic pricing for EV charging stations: A deep reinforcement learning approach. IEEE Trans Transp Electrif 2022;8(2):2456–68.
[23] Liu J, Wang S, Tang X. Cooperative charging stations management under irrational hierarchy EV behaviors. IEEE Internet Things J 2024;11(6):11137–51.
[24] Ajagekar A, You F. Quantum computing for energy systems optimization: Challenges and opportunities. Energy 2019;179:76–89.
[25] Ajagekar A, You F. Quantum computing and quantum artificial intelligence for renewable and sustainable energy: A emerging prospect towards climate neutrality. Renew Sustain Energy Rev 2022;165:112493.
[26] Ajagekar A, Humble T, You F. Quantum computing based hybrid solution strategies for large-scale discrete-continuous optimization problems. Comput Chem Eng 2020;132:106630.
[27] Dalyac C, Henriet L, Jeandel E, Lechner W, Perdrix S, Porcheron M, Veshchezerova M. Qualifying quantum approaches for hard industrial optimization problems. A case study in the field of smart-charging of electric vehicles. EPJ Quantum Technol 2021;8(1).
[28] Sakib N, Chen X. Quantum-powered optimization for electric vehicle charging infrastructure deployment. 2024, arXiv preprint arXiv:2411.06684.
[29] Xu H, Zhang A, Wang Q, Hu Y, Fang F, Cheng L. Quantum Reinforcement Learning for real-time optimization in Electric Vehicle charging systems. Appl Energy 2025;383:125279.
[30] Deng Z, Li Y, Wang X, Jiang Z, Dong B. Quantum computing-enhanced large-scale residential electric vehicle charging management. Appl Energy 2025;401:126772.
[31] Christeson T, Khodaei A, Fan R. Quantum computing for EVs to enhance grid resilience and disaster relief: Challenges and opportunities. 2025, arXiv preprint arXiv:2511.00736.

[32] International Energy Agency (IEA). Global EV outlook 2024: trends in electric cars. Paris, France: IEA; 2024, Available: https://www.iea.org/reports/global-ev-outlook-2024/trends-in-electric-cars.
[33] Ministry of Land, Infrastructure and Transport (MOLIT). Republic of Korea, automobile registration statistics (2024 annual report). Government of the Republic of Korea; 2024, Available: https://www.korea.kr/briefing/pressReleaseView.do?newsId=156611474.
[34] Hyundai Motor Company. IONIQ 5 – technical specifications (Korea catalog). Seoul: Republic of Korea; 2024, Available: https://www.hyundai.com/kr/ko/e/vehicles/ioniq5/spec.
[35] Hyundai Motor Company. IONIQ 6 – technical specifications (Korea catalog). Seoul: Republic of Korea; 2024, Available: https://www.hyundai.com/kr/ko/e/vehicles/ioniq6/spec.
[36] Hyundai Motor Company. KONA electric – Technical specifications (Korea catalog). Seoul: Republic of Korea; 2024, Available: https://www.hyundai.com/kr/ko/e/vehicles/kona-electric/spec.
[37] Kia Corporation. EV6 – Technical specifications (Korea official website). Seoul: Republic of Korea; 2024, Available: https://www.kia.com/kr/vehicles/ev6/features.html.
[38] Kia Corporation. Ray EV – technical specifications (Korea official website). Seoul: Republic of Korea; 2024, Available: https://www.kia.com/kr/vehicles/ray-ev/features.html.
[39] Tesla, Inc. Model 3 – Specifications (Korea market). 2024, Available: https://www.tesla.com/ko_kr/model3.
[40] Tesla, Inc. Model Y – Specifications (Korea market). 2024, Available: https://www.tesla.com/ko_kr/modely.
[41] Tago. 2023 electric vehicle sales ranking in South Korea. 2024, Available: https://tago.kr/model/order.htm.
[42] Chea S. Just one tesla sold in Korea this year as government targets Chinese batteries. Korea JoongAng Daily; 2024, Available: https://koreajoongangdaily.joins.com/news/2024-02-05/business/industry/Just-one-Tesla-sold-in-Korea-this-year-as-govt-targets-Chinese-batteries/1974562.
[43] National Renewable Energy Laboratory (NREL), Hodge C, et al. Electric vehicles as mobile power: technology and grid integration considerations. NREL Technical Report, 2024, Available: https://www.nrel.gov/docs/fy25osti/91358.pdf.
[44] Korea Electric Power Corporation (KEPCO). Electric rates table — electric vehicle charging tariff. KEPCO Official Website; 2025, Available: https://home.kepco.co.kr/kepco/EN/F/htmlView/ENFBHP00108.do?menuCd=EN060201.
[45] Preis V, Biedenbach F. Assessing the incorporation of battery degradation in vehicle-to-grid optimization models. Energy Inform 2023;6:33.
[46] Sagaria S, van der Kam M, Boström T. Vehicle-to-grid impact on battery degradation and estimation of V2G economic compensation. Appl Energy 2025;377:124546.